Electronic Band Tuning and Multivalley Raman Scattering in Monolayer Transition Metal Dichalcogenides at High Pressures

G. Pimenta Martins, Luiz ; R. Carvalho, Bruno ; A. Occhialini, Connor ; Paz Neme, Natália; Park, Ji-Hoon ; Song, Qian ; Venezuela, Pedro ; S. C. Mazzoni, Mário; J. S. Matos, Matheus ; Kong, Jing

Published in:
Acs Nano

DOI:
10.1021/acsnano.2c01065

Publication date:
2022

ACSNANO

www.acsnano.org

ARTICLE

Electronic Band Tuning and Multivalley Raman Scattering in Monolayer Transition Metal Dichalcogenides at High Pressures

Luiz G. Pimenta Martins,* Bruno R. Carvalho, Connor A. Occhialini, Natália P. Neme, Ji-Hoon Park, Qian Song, Pedro Venezuela, Mário S. C. Mazzoni, Matheus J. S. Matos,* Jing Kong,* and Riccardo Comin*

Cite This: *ACS Nano* 2022, 16, 8064–8075

Read Online

ACCESS | Metrics & More | Article Recommendations | Supporting Information

ABSTRACT: Transition metal dichalcogenides (TMDs) possess spin-valley locking and spin-split K/K′ valleys, which have led to many fascinating physical phenomena. However, the electronic structure of TMDs also exhibits other conduction band minima with similar properties, the Q/Q′ valleys. The intervalley K−Q scattering enables interesting physical phenomena, including multivalley superconductivity, but those effects are typically hindered in monolayer TMDs due to the large K−Q energy difference (ΔE_{KQ}). To unlock elusive multivalley phenomena in monolayer TMDs, it is desirable to reduce ΔE_{KQ}, while being able to sensitively probe the valley shifts and the multivalley scattering processes. Here, we use high pressure to tune the electronic properties of monolayer MoS_2 and WSe_2 and probe K−Q crossing and multivalley scattering via double-resonance Raman (DRR) scattering. In both systems, we observed a pressure-induced enhancement of the double-resonance LA and 2LA Raman bands, which can be attributed to a band gap opening and ΔE_{KQ} decrease. First-principles calculations and photoluminescence measurements corroborate this scenario. In our analysis, we also addressed the multivalley nature of the DRR bands for WSe_2. Our work establishes the DRR 2LA and LA bands as sensitive probes of strain-induced modifications to the electronic structure of TMDs. Conversely, their intensity could potentially be used to monitor the presence of compressive or tensile strain in TMDs. Furthermore, the ability to probe K−K′ and K−Q scattering as a function of strain shall advance our understanding of different multivalley phenomena in TMDs such as superconductivity, valley coherence, and valley transport.

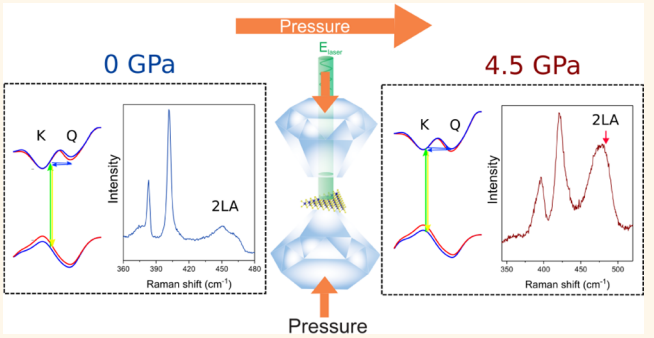

KEYWORDS: *high pressure, TMDs, strain, double-resonance Raman, multivalley physics*

INTRODUCTION

Semiconducting transition metal dichalcogenides (TMDs) MX_2 (M = W, Mo; X = S, Se) host a great variety of intriguing phenomena thanks to their characteristic electronic structures and rich valley physics.[1] A valley is an extreme of the energy dispersion in momentum space, either a local minimum in the conduction band or a local maximum in the valence band, and the valley quantum number labels the valley degree of freedom that is occupied by an electron.[2] In the monolayer limit, semiconducting TMDs exhibit a direct band gap[3] in which the conduction band minima (CBM) and valence band maxima form two valleys at the K/K′ corners of the Brillouin zone (BZ),[4,5] as shown in Figure 1a. The combination of strong spin−orbit coupling (SOC) and broken inversion symmetry locks the spin and valley degrees of freedom together and gives rise to spin-polarized bands at K/K′,[6,7] leading to phenomena such as the valley Hall effect[8,9] and valley Zeeman effect.[10,11]

Besides the well-known valleys at the K/K′ points, MX_2-TMDs also exhibit a second CBM roughly midway between K and Γ points in the BZ. These conduction band extrema are located at the Q-points (also termed Λ points), providing six additional valleys[5,12] as shown in Figure 1a for the monolayer.

Received: January 30, 2022
Accepted: April 21, 2022
Published: April 25, 2022

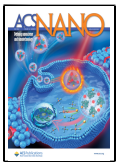

https://doi.org/10.1021/acsnano.2c01065
ACS Nano 2022, 16, 8064−8075

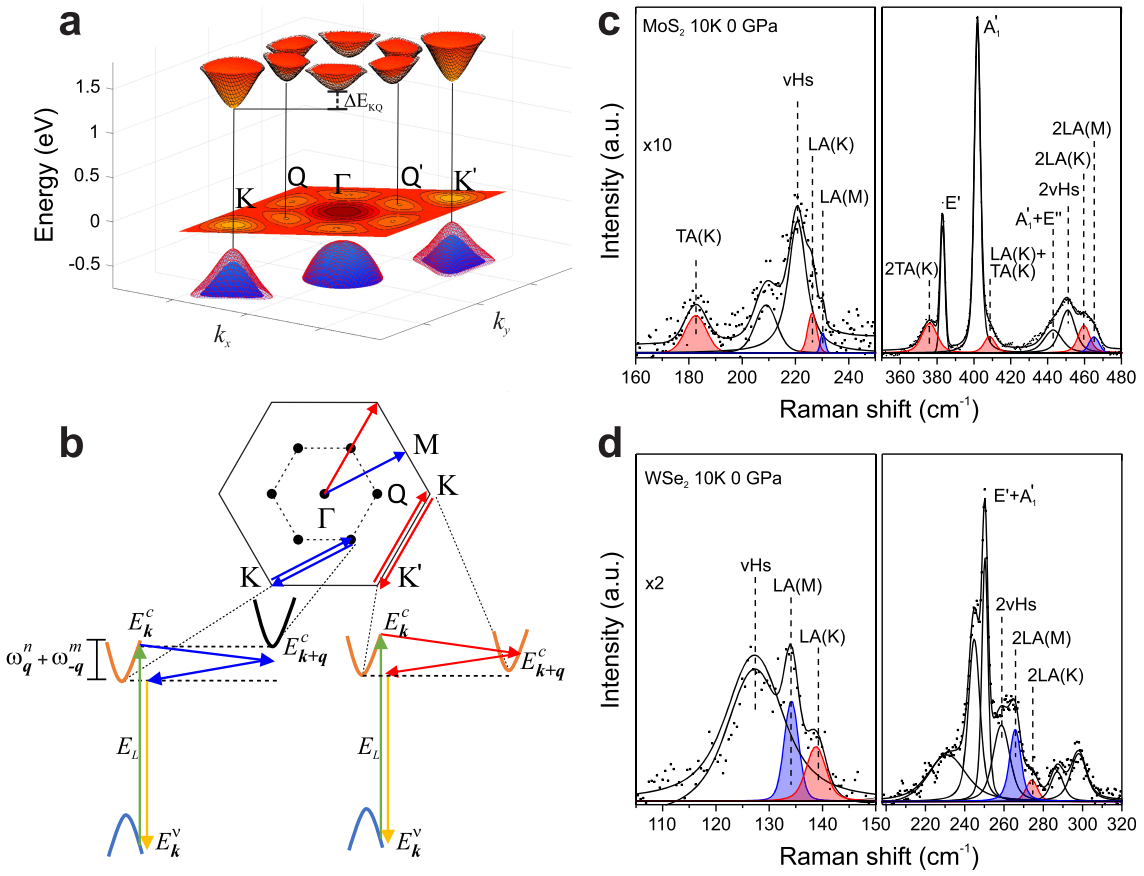

Figure 1. Double-resonance Raman scattering processes for monolayer MoS_2 and WSe_2. (a) Low-energy band structure of monolayer semiconducting TMDs [MX_2 (M = Mo, W; X = S, Se)] near the conduction and valence band edges showing spin-split valleys at the high symmetry K-, Γ-, and Q-points of the BZ zone (here, MoS_2 is chosen as example). The energy difference between K and Q valleys (ΔE_{KQ}) is ~118−246 meV for MoS_2[5,18−20] and ~30−40 meV for WSe_2.[5,20,21] (b) Schematic representation of the two-phonon DRR processes for monolayer MoS_2 and WSe_2 at ambient pressure. Intervalley scattering between K−Q as well as K−K′ valleys can occur. The K−Q scattering is mostly mediated by phonons near M, while K−K′ scattering involves phonons near K. (c, d) Raman spectra of monolayer (c) MoS_2 and (d) WSe_2 acquired at 10 K and 0 GPa conditions, showing the first-order bands and DRR modes involving either two-phonons or one-phonon-one-defect. The spectra were fitted using Voigt functions, with the relevant DRR modes being highlighted in red and blue for K−K′ and K−Q scattering processes, respectively.

Similar to the K/K′ case, the Q/Q′ valleys also exhibit spin-valley locking and spin splitting for odd layers,[4] with the splitting at the Q valley being considerably larger than the one at the conduction band at K.[13] Thus far, the majority of studies on atomically thin TMDs have focused on physical phenomena arising from properties of the K/K′ valleys, while multivalley physics involving both K and Q valleys has been relatively unexplored.

Previous studies have demonstrated the great potential of multivalley physics for TMDs, examples being the observation of the valley Zeeman effect for Q valleys in odd-layer TMDs[4] and the detection of spin-conserving scattering processes involving Q valleys in monolayer WSe_2, which imply long valley and spin lifetime.[13] Furthermore, the electron mobility in TMDs may be significantly affected by K−Q scattering processes, which highly depends on the energy difference between the CBM at K and Q-points (ΔE_{KQ}).[5,14] More recently, it has been shown that the superconductivity observed in ion-gated few-layer semiconducting MoS_2 only occurs when the Fermi level crosses K and both spin-polarized bands at the Q valley.[15,16] The proposed mechanism is an enhancement of the electron−phonon coupling due the combined effects of (i) an increase in the Fermi surface area after Fermi-level crossing of K and Q, forming K/K′ and Q/Q′ electron pockets and (ii) in the number of phonons connecting states in those pockets.[15,17] That is, phonons involved in K−K′, K−Q, and Q−Q scattering.

Despite these important recent developments, the effects of multivalley physics in monolayer TMDs are usually obfuscated by the large value of ΔE_{KQ}: ~118−246 meV for MoS_2[5,18−20] and ~30−40 meV for WSe_2.[5,20,21] Importantly, even though ΔE_{KQ} is smaller for WSe_2, the value of ΔE_{KQ_2}, with Q_2 being the upper spin-polarized band at Q, should be much higher given the large estimated spin split of ~200 meV at Q.[13] Therefore, to unlock elusive multivalley physics phenomena in monolayer TMDs, it is highly desirable to reduce ΔE_{KQ} using an external parameter such as strain or pressure, while simultaneously probing the valley shifts as well as the multivalley scattering processes. High-pressure photoluminescence (PL) experiments using diamond anvil cells (DACs) reported a reduction in ΔE_{KQ}, leading to an eventual K−Q crossing in monolayer TMDs[18,22,23] in the 0−4 GPa range. Even though those works provided strong evidence of such crossing, PL itself is not an ideal probe of band crossing in strained TMDs given the possible overlapping contribution from optical transitions at different locations in the BZ.

https://doi.org/10.1021/acsnano.2c01065
ACS Nano 2022, 16, 8064−8075

Furthermore, PL measurements are not able to directly probe multivalley scattering processes.

In this context, double-resonance Raman (DRR) scattering is a powerful probe of the electronic structure and intervalley scattering processes in 2D materials,[24] as has been well-established for graphene[25] and, more recently, for monolayer MoS_2.[19] Furthermore, DRR scattering is also sensitive to band structure modifications in 2D materials, being able to detect doping effects,[26,27] defect levels,[28,29] and strain.[30,31] Nevertheless, to the best of our knowledge, there are no reports of probing strain-induced modifications in the electronic structure of TMDs via DRR spectroscopy.

In the present study, we compressed monolayer MoS_2 and WSe_2 at high pressures (0−4.5 GPa) and low temperatures (10 K) while probing K−Q crossing and multivalley scattering via DRR scattering. In both systems, we observed a pressure-induced enhancement of the double-resonance LA and 2LA Raman bands. Such an enhancement can be attributed to the combined effects of a K−Q crossover in the electronic dispersion and a blueshift of the B exciton energy closer to the fixed laser excitation energy, with increasing pressure. Such a scenario is confirmed by PL measurements and density functional theory (DFT) calculations. The combination of PL and DRR measurements provides robust evidence of K−Q crossing. We also address the multivalley nature of the modes originated from the DRR scattering processes for WSe_2. Our work establishes the DRR 2LA and LA bands as sensitive probes of strain-induced modifications to the electronic structure of TMDs. Hence, the intensity and shape of the DRR bands can be used as means to monitor the presence of compressive or tensile strain in TMDs. Furthermore, the ability to tune ΔE_{KQ} and probe K−K′ and K−Q scattering processes as a function of strain is key to capture and enhance different multivalley phenomena in TMDs such as valley coherence, valley transport,[5,14] and superconductivity.[17]

RESULTS AND DISCUSSION

We initially discuss the scattering processes that give rise to the DRR bands for monolayer MoS_2 and WSe_2. In these events, the scattering of electrons (or holes) is mediated by two phonons, or by a phonon and a defect. Figure 1b schematically describes the DRR scattering of electrons by two-phonon processes in the single-particle picture (see ref 19 for the equivalent excitonic description). The electronic dispersions near the K and Q valleys are represented by parabolic bands with spin splitting omitted for clarity. For both events, the scattering process begins with the absorption of a photon with energy E_L and creation of an electron−hole pair near the K-point (equivalent discussion follows for absorption at K′). The energy of the electron−hole pair ($E_{\mathbf{k}}^{eh}$) is then $E_{\mathbf{k}}^{c}-E_{\mathbf{k}}^{v}$, where $E_{\mathbf{k}}^{c}$ ($E_{\mathbf{k}}^{v}$) is the energy of electron with momentum $\mathbf{k}$ near the K-point and c (v) is the conduction (valence) band. The excited electron is then inelastically scattered to either the K′ or Q valley upon creation of a phonon with momentum $\mathbf{q}$ and energy $\hbar\omega_{\mathbf{q}}^{n}$ (n is the phonon branch), to an intermediate state with energy $E_{\mathbf{k}+\mathbf{q}}^{c}$. To conserve momentum, the electron is inelastically scattered back to K by the creation of a second phonon with momentum $-\mathbf{q}$ and energy $\hbar\omega_{-\mathbf{q}}^{m}$. Phonons involved in K−K′ (K−Q) scattering processes are represented with red (blue) arrows, and their loci are around the K (M) points in the BZ,[19] as shown in Figure 1b by translating those vectors to the Γ point. The electron−hole pair then recombines at K and a photon with energy $E_L - \hbar\omega_{\mathbf{q}}^{n} - \hbar\omega_{\mathbf{q}}^{m}$ is emitted. Whenever the electronic transitions occur between real states (instead of virtual states), the overall four-stage process is resonant, leading to a significant enhancement in the intensity of the Raman signal. The resonant condition can be represented by arrows connecting real states in the scattering process (see Figure 1b for a double-resonant K−K′ process).

This enhancement can be quantified by analyzing the intensity for a second-order Raman process, given by[32]

$$I \propto \left| \sum_{\mathbf{k},\mathbf{q},m,n} \frac{\langle f|H_{er}|c\rangle\langle c|H_{ep}|b\rangle\langle b|H_{ep}|a\rangle\langle a|H_{er}|i\rangle}{(E_L - E_{\mathbf{k}}^{eh} - i\epsilon)(E_L - E_{\mathbf{k}+\mathbf{q}}^{c} + E_{\mathbf{k}}^{v} - \hbar\omega_{\mathbf{q}}^{n} - i\epsilon)(E_L - E_{\mathbf{k}}^{eh} - \hbar\omega_{\mathbf{q}}^{n} - \hbar\omega_{-\mathbf{q}}^{m} - i\epsilon)} \right|^2 \quad (1)$$

where $\langle a|H_{er}|i\rangle$ and $\langle f|H_{er}|c\rangle$ are the matrix elements for absorption and emission of a photon, respectively, and $\langle c|H_{ep}|b\rangle$ and $\langle b|H_{ep}|a\rangle$, are the matrix elements for the electron−phonon coupling involved in the intermediate scattering processes. The parameter ϵ is a damping constant associated with the finite lifetime of the intermediate states. The double-resonance phenomena condition will occur whenever two terms of the denominator in eq 1, apart from the damping terms, are zero.

Figure 1c,d exhibits the Raman spectra obtained from monolayer CVD MoS_2 and WSe_2 samples, respectively, acquired at 10 K and ambient-pressure conditions using a 2.33 eV laser excitation. The spectra were fitted using Voigt functions (see Methods). In Figure 1c, one can observe two prominent features around 383 and 402 cm^{-1} which correspond to the first-order in-plane and out-of-plane E' and A'_1 modes, respectively. Additionally, a broad feature in the 430−470 cm^{-1} range has been generically termed as the 2LA band in the literature;[20,33] however, this broad band is composed of several two-phonon DRR processes with phonons located at different points within the BZ.[19] Here, the mode assignment for the 2LA band in MoS_2 follows the conclusions of ref 19.

The mode located near 443 cm^{-1} corresponds to the scattering of one A'_1 and one E' phonon at the Γ point; thus, we label it as $A'_1(\Gamma) + E'(\Gamma)$. The peak at 451 cm^{-1} is associated with scattering by two phonons due to a van Hove singularity (vHs) at the saddle-point in the phonon density of states, which is located between the K and M points of the longitudinal acoustic (LA) phonon branch (see Supporting Figure S1) and thus is labeled as 2vHs. The peak at approximately 460 cm^{-1} corresponds to K−K′ scattering by two-LA-phonons, with phonon locus near K-point (see red arrows in Figure 1b), assigned as 2LA(K). Finally, the peak at approximately 465 cm^{-1} corresponds to K−Q scattering by two LA-phonons located near the M point (see blue arrows in Figure 1b), assigned as 2LA(M).

https://doi.org/10.1021/acsnano.2c01065
ACS Nano 2022, 16, 8064−8075

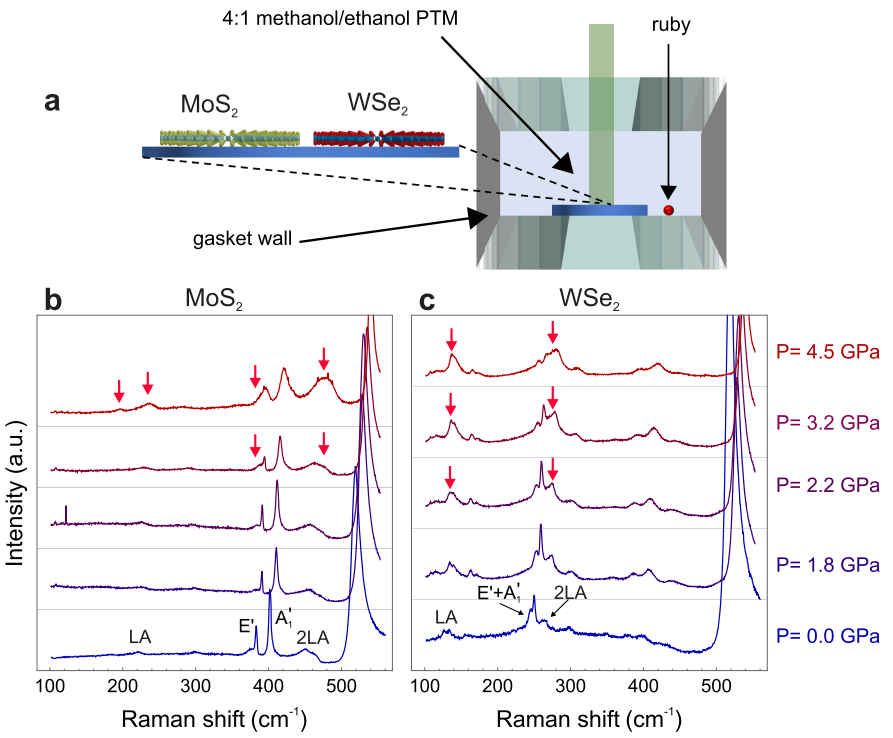

Figure 2. Pressure-induced enhancement of DRR modes. (a) Schematics of the high-pressure Raman and photoluminescence experiment using a 2.33 eV excitation laser. WSe_2 and MoS_2 monolayer CVD samples were prepared onto the same SiO_2/Si substrate and loaded into the DAC using the horseshoe method.[37] Pressure was determined in situ from a low-temperature ruby fluorescence calibration,[41] and a 4:1 methanol/ethanol mixture was used as the PTM. (b, c) Raw Raman spectra of MoS_2 (b) and WSe_2 (c) as a function of pressure and at 10 K. Modes that are relevant to our analysis are labeled at the bottom spectra for each system. Red arrows highlight the enhancement of the DRR modes with pressure.

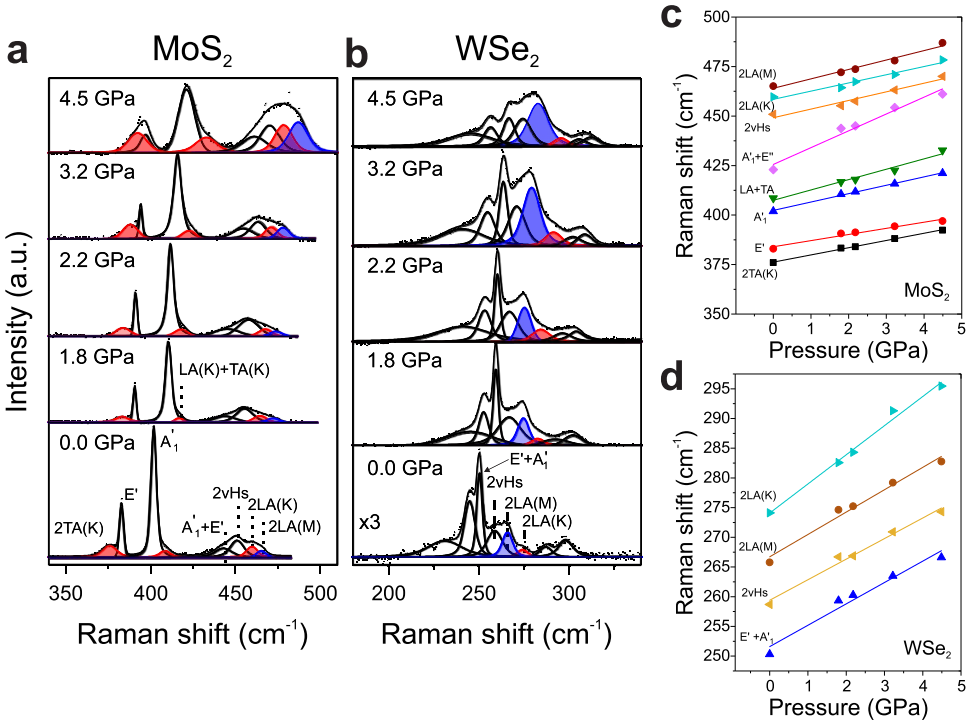

Figure 3. Pressure-evolution of Raman modes. (a, b) Raman spectra of MoS_2 (a) and WSe_2 (b) in the range of the first-order and DRR 2LA bands at increasing pressures fitted using Voigt functions (see Methods). Relevant DRR modes are highlighted in red (K−K′ scattering) and blue (K−Q scattering). For MoS_2 (WSe_2), the two-phonon DRR modes are labeled at the bottom spectrum in a (b). (c, d) Raman frequencies as a function of pressure for monolayer MoS_2 (c) and WSe_2 (d). The linear behavior observed in both systems is a good indicator of the absence of inhomogeneous strain.

https://doi.org/10.1021/acsnano.2c01065
ACS Nano 2022, 16, 8064−8075

As recently reported,[34] the peak at approximately 376 cm^{-1} is also associated with K−K′ scattering, however, the electrons are scattered by two transverse acoustic (TA) phonons instead, thus assigned as 2TA(K). The shoulder on the right-side of the A'_1 mode corresponds to a band that is associated with K−K′ scattering processes involving one LA and one TA phonon with opposite momenta near the K-point, thus assigned as LA(K)+TA(K).[19]

In the 160−250 cm^{-1} range of the MoS_2 spectra (Figure 1c), we can observe the TA(K), vHs, LA(K), and LA(M) bands, exhibiting approximately half of the frequencies of the previously mentioned DRR features. Those are defect-activated Raman bands (similar to the D band in graphene[28]) originating from DRR processes in which the excited electron at K is scattered to a different valley (K′ or Q) by emission of a phonon and then elastically scattered back to K, ensuring momentum conservation.[19]

The most prominent feature in the Raman spectrum of monolayer WSe_2, shown in Figure 1d, corresponds to the nearly doubly degenerate first-order band at approximately 250 cm^{-1} assigned as the $E' + A'_1$ mode at the Γ point. Several reports refer to the band in the 260−280 cm^{-1} as the 2LA(M) band,[20,35,36] that is, involving K−Q scattering processes. However, to the best of our knowledge, the detailed scattering processes that give rise to this band are still elusive, which we elucidate here with the aid of first-principle calculations. The 2LA band is deconvolved into three peaks located around 258, 265, and 274 cm^{-1}, which we assign as 2vHs, 2LA(M), and 2LA(K), respectively (Figure 1d). This assignment is based on the calculated phonon dispersion of monolayer WSe_2 and its resemblance to MoS_2[19] (see Supporting Note S1). The defect-activated band appears in the 110−150 cm^{-1} range where the phonon frequencies of the peaks are approximately half of those for the 2LA bands. We therefore label these peaks appropriately as vHs, LA(M), and LA(K). Finally, we highlight additional features appearing below 250 cm^{-1} and above 280 cm^{-1} that require further investigation.

High-pressure Raman and PL experiments were performed on CVD MoS_2 and WSe_2 monolayers, transferred onto the same SiO_2/Si substrate and loaded into a DAC using the horseshoe method[37] (see Methods). A schematic of the setup is shown in Figure 2a. At each pressure, we collected Raman and photoluminescence spectra of the isolated flakes using a 2.33 eV excitation laser and at a temperature of 10 K (see Methods). The high-pressure experiments were performed at low-temperature conditions to better resolve the PL features; however, we point out that similar results should be observed at ambient temperature. A mixture of 4:1 methanol/ethanol was used as the pressure transmitting medium (PTM).

Figure 2b,c shows the raw Raman spectra of MoS_2 (Figure 2b) and WSe_2 (Figure 2c) for increasing pressures up to 4.5 GPa. Here, we focus our analysis on the first-order Raman modes: E' and A'_1 for MoS_2 and $E' + A'_1$ for WSe_2; and on the DRR modes: LA and 2LA, both present in the Raman spectra of each flake. As expected, the frequencies of all modes blueshift with increasing pressure, due to a phonon hardening induced by the compressive strain.[38] One can also observe the enhancement in intensity of the LA and 2LA bands as pressure increases, becoming well-pronounced above 3.2 GPa (2.2 GPa) for MoS_2 (WSe_2) (see red arrows in Figure 2b,c).

Figure 3a,b shows the fitted Raman spectra of monolayer MoS_2 (Figure 3a) and WSe_2 (Figure 3b) from Figure 2b,c, in the spectral range of the first order and 2LA modes and as a function of pressure (see Supporting Figure S2 for the LA bands). For both materials, the intensity of all DRR modes is enhanced when compared to the first-order bands and to the Raman peak from the silicon substrate (see Supporting Figure S3). For MoS_2 (Figure 3a), we note a clear enhancement of the 2TA(K) and LA(K) + TA(K) modes in addition to the 2LA modes. The same trend is observed for the DRR 2LA(K) and 2LA(M) modes in monolayer WSe_2 (Figure 3b). The pressure-enhancement is also apparent for single-phonon LA(K) and LA(M) modes in both MoS_2 and WSe_2 (see Supporting Figure S2).

Figure 3c,d summarizes the pressure evolution of the Raman frequencies for the 2TA(K), E', A'_1, and 2LA modes for MoS_2 (Figure 3c) and for the $E' + A'_1$ and 2LA modes for WSe_2 (Figure 3d). Notice that all modes for both systems exhibit a linear behavior.

We now discuss the proposed mechanism behind the pressure-induced enhancement of the DRR LA and 2LA bands. Since the LA band is defect-activated, one may hypothesize that its enhancement is associated with an increasing disorder in the system as pressure increases. While disorder could arise, for instance, from non-hydrostatic effects, several aspects indicate that increasing disorder effects are negligibly small if present. These aspects include (i) the linear pressure evolution of the Raman frequencies (Figure 3c,d)—deviations from linear behavior are expected under the presence of shear components,[39] (ii) the choice of the 4:1 methanol/ethanol PTM, which is a good PTM for our pressure−temperature range,[40,41] and (iii) the spatial homogeneity of Raman signal at maximum pressure (see Supporting Note S4 for detailed discussion).

Most importantly, the clearest evidence for the lack of a significant increase in disorder is that the enhancement of the LA band is accompanied by an enhancement of the 2LA band, as can be seen in Figure 2b,c. If disorder was increasing in those systems, the 2LA band intensity should decrease and eventually vanish for increasing defect density, as observed for MoS_2[42,43] and for the 2D band in graphene.[44] Thus, the changes we observed for the DRR modes cannot be explained by increasing disorder. The broadening observed for the first-order Raman bands for MoS_2 and WSe_2 is likely associated with the proximity with the resonance conditions (see Supporting Note S10 after discussion of the K−Q crossing and blueshift of B exciton energy in the main text).

Therefore, we can confidently attribute the enhancement of the DRR modes to the combined pressure-induced effects of (i) a crossing of the K and Q valleys in the electronic band structure; and (ii) a blueshift of the B exciton energy, becoming closer to the laser excitation energy with increasing pressure. We start by discussing the first effect.

The contribution of the K−Q scattering process to the 2LA and LA bands for monolayer MoS_2 and WSe_2 is generally weak at ambient pressure due to the large energy mismatch between the K- and Q-band minima.[19] This can be understood from Figure 1b, where a possible scattering process from K to Q involves a virtual intermediate electronic state (corresponding to the second term in the denominator of eq 1 significantly deviating from zero). However, if K and Q valleys become progressively closer in energy, which is the case when the number of layers increases in both MoS_2 and WSe_2, the K−Q scattering contribution to the intensity of the DRR processes is resonantly enhanced, as observed for MoS_2.[19] In this context, it has been reported that pressure reduces the energy difference

https://doi.org/10.1021/acsnano.2c01065
ACS Nano 2022, 16, 8064−8075

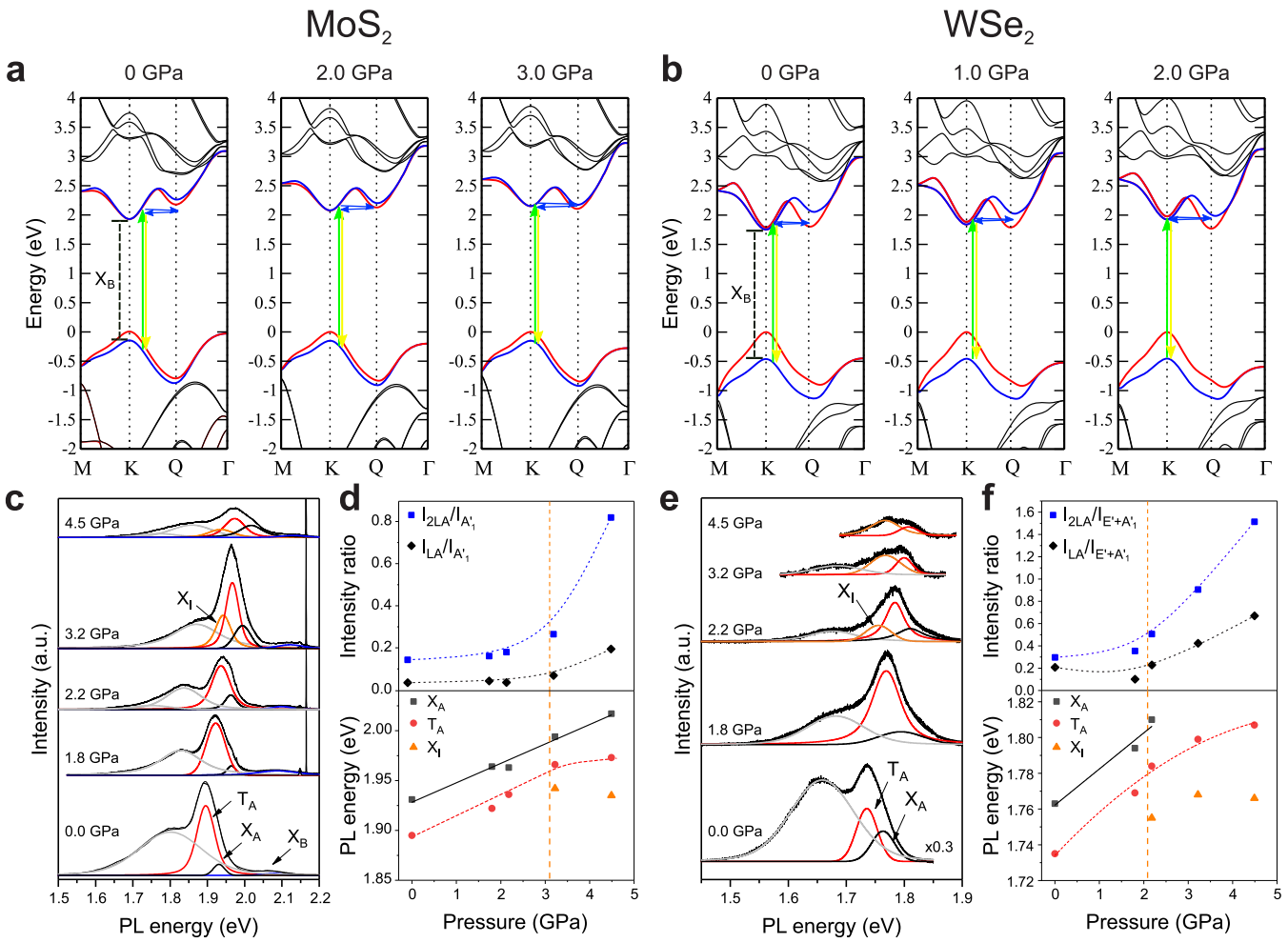

Figure 4. K−Q crossing with increasing pressure. (a, b) Calculated electronic band structure for MoS_2 (a) and WSe_2 (b) as a function of pressure. Spin-down (spin-up) bands are highlighted in red (blue). The arrows represent the photon absorption process for 2.33 eV photoexcitation, and subsequent K−Q scattering processes and exciton recombination. (c, e) Photoluminescence spectra taken with increasing pressures for MoS_2 (c) and WSe_2 (e) at 10 K using 2.33 eV excitation laser. The A exciton (X_A), A trion (T_A), and B exciton (X_B) peaks are labeled at the bottom spectra in each figure. (d, f) Intensity ratio of the 2LA and LA bands by the A'_1 mode for MoS_2 (d - top panel) and the $E' + A'_1$ band for WSe_2 (f - top panel). The vertical dotted lines in (d, f - top panels) mark the sudden increase in the normalized intensity of the DRR modes. Notice that the enhancement of those modes occurs at lower pressures for WSe_2 compared to MoS_2, in qualitative agreement with K−Q crossing from DFT calculations. (d, f - bottom panels) show the energies of T_A, X_A, and X_I peaks extracted from the spectra in (c, e) as a function of pressure for MoS_2 (d) and WSe_2 (f). The vertical dotted lines in (d, f -bottom panels) mark the deviation from the linear behavior in the pressure dependence of trion peak (T_A) and the rise of the lower energy peak X_I.

between K and Q valleys in TMDs, leading to an eventual K−Q crossing.[18,22,23]

To corroborate the above reasoning and better understand the physical mechanisms involved in the DRR processes, we performed first-principles DFT calculations, assessing the electronic and vibrational properties of 2D-TMDs subjected to hydrostatic pressure (see Methods). Figure 4a,b displays the calculated band structures with increasing pressure for MoS_2 (Figure 4a) and WSe_2 (Figure 4b). At ambient pressure, MoS_2 (Figure 4a, left panel) has a direct band gap at the K-point, and the energy difference between the band minima at K and Q is ∼0.25 eV. The bands highlighted in red and blue correspond, respectively, to spin-down and spin-up states,[5] and reveal a spin splitting of approximately ∼85 meV at Q. These bands become spin polarized when the effect of the spin orbit coupling in the conduction bands is taken into account, as done in ref 5. At 2 GPa (Figure 4a, center panel), the two minima become degenerate within 0.05 eV—at this point the K−Q crossing takes place, making the band gap indirect upon a further increase in pressure, as shown in the right panel. Figure 4b shows the same trend for WSe_2. However, the K−Q crossing occurs for a pressure slightly lower than 1 GPa for the lower spin-polarized band at Q. Notice that the ambient-pressure spin splitting at Q for WSe_2 is considerably larger, around ∼250 meV. The threshold pressure to trigger the transition is in excellent agreement with other theoretical predictions.[18,23]

Our calculations indicate that the K−Q transition is due to a pressure-induced in-plane compression, and it is explained by the character of the atomic orbitals which build up the states at the bottom of the conduction band at the K- and Q-points. Indeed, while the predominant contribution at the K-point comes from the molybdenum $4d_{z^2}$ orbitals, at the Q-point the most important orbitals are in-plane molybdenum d orbitals, $4d_{x^2-y^2}$ and $4d_{xy}$. Upon decreasing the lattice parameter, the deformation has a larger effect in the states built upon the in-plane orbitals, and the net result is a decrease in the energy of

https://doi.org/10.1021/acsnano.2c01065
ACS Nano 2022, 16, 8064−8075

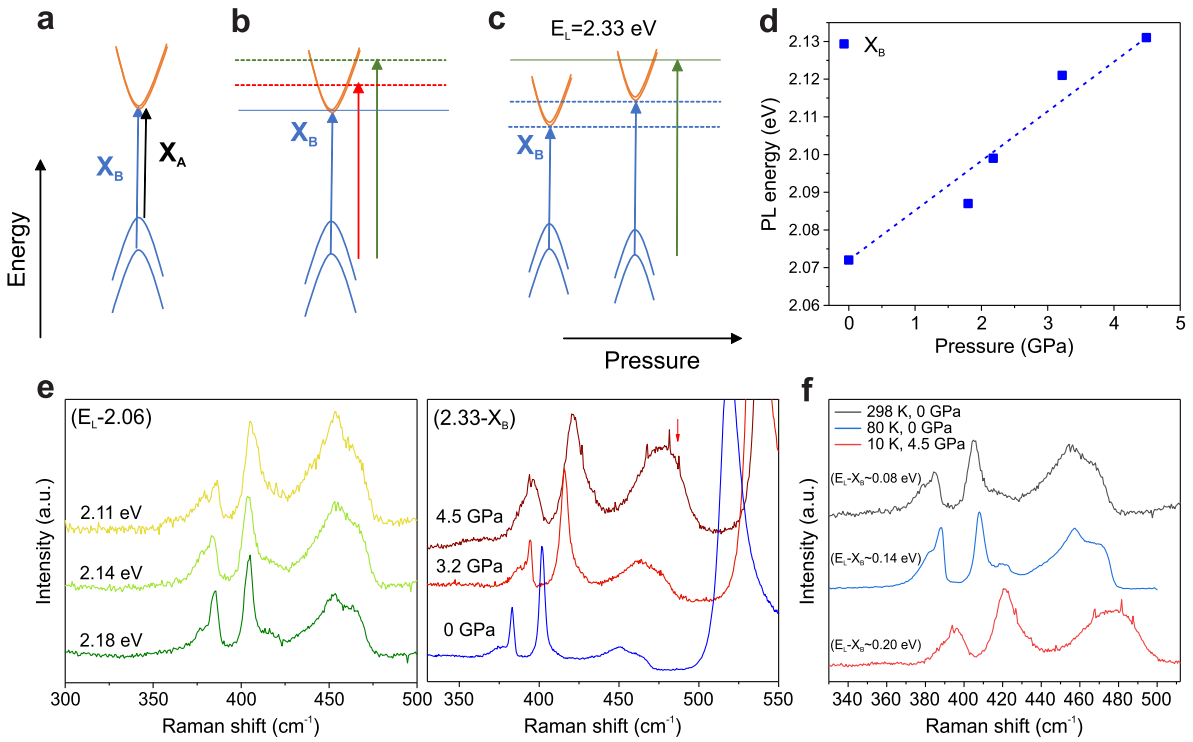

Figure 5. Blueshift of the B exciton energy with increasing pressure. (a) Illustration of the 1s excitonic transitions from the spin-split valence band to the conduction band at K/K′ in monolayer TMDs associated with the A and B excitons, with energies X_A and X_B, respectively. (b) Diagram illustrating the process of approaching the resonance condition $(E_L - X_B) \rightarrow 0$ from above, by reducing E_L for a fixed X_B. Excitation energies are represented by the green and red arrows. (c) Diagram representing the process of approaching the resonance condition $(E_L - X_B) \rightarrow 0$ from above, by fixing E_L and blueshifting X_B as pressure increases. (d) B exciton energy X_B for MoS_2 as a function of pressure. (e) Comparison between the Raman spectra from ref 19 of monolayer MoS_2 acquired with different laser excitations at ambient temperature and pressure conditions (left panel) with our Raman data acquired with 2.33 eV excitation energy at 10 K for increasing pressure (right panel). (f) Raman spectra showing similar features for the DRR modes measured under different ambient conditions and their values for $E_L - X_B$. Top spectra: 2.14 eV excitation at ambient temperature and pressure, obtained from ref 19. Middle: 2.21 eV excitation at 80 K and ambient pressure, obtained from ref 34. Bottom: 2.33 eV at 10 K and 4.5 GPa.

the Q-point state, which, eventually, becomes lower in energy than the state at the K-point.

Figure 4a,b also highlights the DRR processes represented in Figure 1b for an energy excitation of 2.33 eV. The process depicted focuses on photon absorption near the B exciton energy (X_B) due to its proximity to our laser excitation energy and to the significant difference between the 2LA band intensity near A and B exciton energies for monolayer MoS_2, with the Raman intensity being much stronger for the latter case.[19] In our analysis, only spin-conserving processes should be considered, that is, transitions from red to red or blue to blue bands in Figure 4a,b. Optical transitions involving spin-flip are either forbidden or weakly allowed,[45] and intervalley scattering processes that require spin flips are inefficient.[13,46] Therefore, the contribution of DRR processes that do not conserve the spin angular momentum should be negligible. Since we are looking for transitions near B exciton energies, as previously explained, we will focus on transitions between blue to blue bands in Figure 4a,b.

It is worth noting that at ambient pressure, the K−Q scattering process involves virtual states near the Q valley for MoS_2 (Figure 4a, left panel), while for WSe_2 it involves real states near Q (Figure 4b, left panel). However, for WSe_2, those states have opposite spin (phonons connect spin-up states at K with spin-down states at Q in Figure 4b, left panel) for an absorption closer to X_B. The required spin flip should reduce the probability of those scattering events and their contribution to the DRR processes in WSe_2. Within the proximity of K- and Q-band minima and the eventual K−Q crossing (center and right panels in Figure 4a,b), there is an increasing contribution of spin-conserving K−Q intervalley scattering processes (blue to blue) near the resonance condition involving real states near Q, leading to an enhancement of the Raman intensity of the DRR modes according to eq 1.

This enhancement can be seen in Figure 4d,f (top panels), which show the intensity ratio of the LA and 2LA bands normalized by the A'_1 mode for MoS_2 (Figure 4d) and the $E' + A'_1$ mode for WSe_2 (Figure 4f). For simplicity, we fitted the 2LA, LA bands with a single Voigt peak for MoS_2, while for WSe_2 we considered the 2LA(M), LA(M) bands since they were the most intense component. The same trend was observed for the normalized pressure evolution for the individual components (see Supporting Figure S5). Notice that the enhancement of the DRR bands, marked by the orange-dotted vertical lines, occurs at a higher pressure for MoS_2 compared to WSe_2, in agreement with the behavior for the K−Q crossing from the theoretical calculations. From Figure 4d,f (top panels), it is possible to infer the critical pressures of ~2 GPa for WSe_2 and of ~3 GPa for MoS_2. Those values are in a good agreement with the range of critical pressures obtained for K−Q crossing from high-pressure PL experiments for different monolayer TMDs: 2.2 GPa for WSe_2,[22] 1.9 GPa for MoS_2,[18] and 3.7 GPa for $MoSe_2$.[23]

https://doi.org/10.1021/acsnano.2c01065
ACS Nano 2022, 16, 8064−8075

The K−Q crossing around those pressures was also confirmed by our PL measurements. Figure 4c,e shows the PL spectra for monolayer MoS_2 (Figure 4c) and WSe_2 (Figure 4e) as a function of pressure. The A exciton (X_A), A trion (T_A), and B exciton (X_B) peaks found from fitting the PL spectra are labeled in each figure (for WSe_2, it was not possible to detect the X_B peak given its weak signature at low temperatures). It is important to point out that at low temperatures, the spectra should be dominated by trions, with our PL energies for T_A and X_A for both materials being in good agreement with values from the literature.[47]

Consistent with previous high-pressure studies for MoS_2[38] and WSe_2,[22] we observed an overall blueshift of the PL with increasing pressure for both materials. Notice that there is a significant broadening of the PL at 3.2 GPa for MoS_2, with an extra peak termed X_I being found in the PL spectra at 3.2 GPa. For WSe_2, the broadening is less pronounced, but the extra peak, also termed X_I, is found above 2.2 GPa, while the PL becomes weaker and its shape progressively more left-skewed. The appearance of the extra peak X_I around those pressures for both MoS_2 and WSe_2 is consistent with a phonon-assisted photoluminescence process from momentum-dark K−Q excitons.[46] A similar Q−K PL peak has been reported for room-temperature compressed $MoSe_2$ monolayer after K−Q crossing.[23] Furthermore, the overall tendency of PL quenching is consistent with K−Q crossing as observed in previous works[18,23,38] (see Supporting Figure S6).

Figure 4d,f - bottom panels shows the energy of T_A, X_A, and X_I peaks as a function of pressure for MoS_2 (Figure 4d) and WSe_2 (Figure 4f). Notice that the X_A energy increases with pressure in a linear fashion (the X_A peak is no longer detectable for WSe_2 above ∼3 GPa). However, the pressure evolution of T_A slightly deviates from linear behavior above 3 GPa for MoS_2, and above 2 GPa for WSe_2. This deviation is marked by orange-dotted lines in Figure 4d,f (bottom panels), which also signal the rise of the lower energy peak X_I. Such deviation of the T_A peak from the linear behavior has been previously observed in compressed TMDs and attributed to the mixing between K and Q states upon K−Q crossover.[18,22]

By inspection of Figure 4d,f, one observes a clear correlation between the PL signatures of K−Q crossing at ∼3 GPa for MoS_2 and at ∼2 GPa for WSe_2, and the enhancement of the LA and 2LA bands at those same pressures. Furthermore, from the combined information presented in Figure 4b,e,f, we point out that for WSe_2, the K−Q crossing at ∼2 GPa should occur between K and the upper spin-polarized band at Q (see Figure 4b -right panel and Supporting Note S7).

Importantly, even though the enhancement of the 2LA(M) mode (K−Q scattering) is comparatively larger than the enhancement of the other DRR modes for both MoS_2 and WSe_2 (see Supporting Figure S5), there is an increase in the intensity of all DRR modes, including those related to K−K′ scattering. This brings us to the second proposed reason for the enhancement of the DRR bands: the blueshift of the B exciton energy.

In a Raman scattering process, a resonant absorption (emission) condition occurs whenever the excitation energy of the photon matches the energy of the electron−hole pair created (recombined)—or the exciton energy in the case of TMDs. This condition sets the first (last) term in the denominator of eq 1 to zero, apart from the damping constant, enhancing the transition probability for this process. In semiconducting TMDs, the A and B excitons are associated with the 1s excitonic transitions from the spin-split valence band to the conduction band, as represented in Figure 5a.

In particular, resonant Raman studies using different excitation energies demonstrated a significant enhancement of the 2LA band for MoS_2[19] and WSe_2[36] upon leveling between the excitation energy (E_L) and the B exciton energy (X_B), this situation being illustrated in Figure 5b. Similarly, we propose that a complementary reason for the enhancement of the DRR features in our work is due to a proximity to the resonance condition: $(E_L - X_B) \rightarrow 0$, with increasing pressure. In the present case, instead of tuning E_L while X_B is fixed, we have a pressure-induced blueshift of X_B for a fixed E_L, as represented in Figure 5c. Such a blueshift of X_B for MoS_2 is shown in Figure 5d.

Figure 5e shows the correspondence between tuning E_L for fixed X_B (left-side panel) and the case when fixing E_L while tuning X_B (right-side panel) by comparing the Raman spectra of monolayer MoS_2 for different laser excitation energies (left panel) measured at ambient conditions (reproduced from ref 19) with our Raman results for different pressures acquired for a fixed 2.33 eV excitation energy (right panel). Notice that there is a resemblance between the spectra in both cases as $E_L - X_B$ gets reduced, with E_L approaching X_B from above. For instance, the Raman spectra measured with an excitation energy of 2.14 eV resembles the Raman spectra measured at 4.5 GPa. Figure 5f compares the aforementioned spectra with the Raman spectrum of monolayer MoS_2 at 80 K and ambient pressure using a 2.21 eV laser excitation, obtained from ref 34. Despite the similarity between the Raman features in the three spectra, the value of $E_L - X_B$ is quite different: approximately 0.08, 0.14, and 0.20 eV for the spectra measured with 2.14 eV excitation at ambient temperature and pressure, 2.21 eV excitation at 80 K and ambient pressure, and 2.33 eV at 10 K and 4.5 GPa, respectively. Therefore, care must be taken for making quantitative one-to-one correspondences between $E_L - X_B$ values and the Raman spectra at different pressures (P) and temperatures (T) since the different PT conditions should affect the resonance Raman excitation profile near the B exciton energy in complex ways. The point here is to show that our hypothesis of proximity of the B exciton resonance with increasing pressure as a complementary cause for the enhancement of the DRR modes is justified by comparing our $E_L - X_B(P)$ energy range to the literature and noting the resemblance between the respective Raman features.

The intensity of the B exciton peak for WSe_2 was too weak to be detected in our low-temperature experiments (see full discussion in Supporting Note S8); therefore, our analysis focused solely on MoS_2. However, even though the X_B peak was not detectable for WSe_2, the implication that it blueshifts is clear if one looks at the X_A pressure evolution (Figure 4f).

Most importantly, we emphasize that it is the combined effect of K−Q crossing and blueshift of B exciton that is the main mechanism responsible for the pressure-induced enhancement of the DRR bands. The proximity to the B exciton resonance should favor the enhancement of all features,[19] while K−Q crossover should selectively enhance the M-phonon modes. In fact, the symmetrical shape of the 2LA band for MoS_2 at maximum pressure (notice the extra spectral weight of the 2LA band indicated by the red arrow in Figure 5e) is an indication of the combination of these two factors (see detailed discussion in Supporting Note S9). This feature could be justified by the increasing contribution of the K−Q scattering process to the 2LA band intensity upon K−Q

https://doi.org/10.1021/acsnano.2c01065
ACS Nano 2022, 16, 8064−8075

crossing, which would change the shape of this band since the 2LA(M) mode—the specific mode associated with K−Q scattering—has the highest frequency among the four modes composing the 2LA band. And as can be seen in Figure 3a and in Supporting Figure S5, the 2LA(M) mode becomes most intense at the highest pressure.

Additional mechanisms to the observed pressure-induced enhancements of DRR bands, such as a possible increase in the phonon density of states or in the contributions from the matrix elements in eq 1, should not have a significant contribution (see Supporting Note S11).

CONCLUSIONS

We investigated the pressure-induced strain evolution of the electronic band structure in monolayer MoS_2 and WSe_2 at high pressures (0−4.5 GPa) and low temperatures (10 K) via DRR scattering while probing multivalley K−K′ and K−Q scattering. In both systems, we observed a pressure-induced enhancement of the DRR modes, mainly LA and 2LA modes. We attributed the enhancement to the combined pressure-induced effects of a crossover between K and Q valleys and a blueshift of the B exciton energy—becoming closer to the laser excitation energy. First-principles calculations and PL measurements corroborate this scenario. In this work, we also addressed the DRR bands in monolayer WSe_2, properly assigning the LA and 2LA bands.

Our results establish DRR spectroscopy and the 2LA band as a sensitive probe of the effects of strain in the electronic properties of TMDs. We anticipate that the analysis we developed for MoS_2 and WSe_2 could in principle be extended to other semiconducting monolayer MX_2 TMDs due to the similarities in their band structure—the presence of spin-split and spin-valley locked K/K′ and Q/Q′ valleys[5]—and in their phonon dispersions along K−M for the LA branch,[48,49] which would result in a similar phenomenology for the DRR processes. Even though observed at high pressures, the phenomena of band gap opening (closing) and decrease (increase) in ΔE_{KQ} has also been predicted for biaxial compressive (tensile) strain in monolayer MX_2.[50] Therefore, it can be inferred that under tensile strain, one should expect the opposite behavior for the LA and 2LA bands as observed in our work: an intensity decrease for a fixed energy excitation. Thus, the intensity and shape of the 2LA and LA bands could potentially be used to monitor the presence of compressive or tensile strain in TMDs. Furthermore, our work should shed light on multivalley physics in TMDs, a relatively unexplored territory, which could be investigated via strain engineering of TMDs for both fundamental studies and for practical valleytronics applications.

METHODS

Synthesis of MoS_2 and WSe_2 Monolayers. Monolayer MoS_2 and WSe_2 flakes were grown under low pressure by metal−organic chemical vapor deposition (MOCVD).[51] Molybdenum hexacarbonyl ($Mo(CO)_6$, Sigma-Aldrich), tungsten hexacarbonyl ($W(CO)_6$, Sigma-Aldrich), diethyl sulfide ($(C_2H_5)_2S$, Sigma-Aldrich), and dimethyl selenide ($(CH_3)_2Se$, Sigma-Aldrich) were selected as precursors of Mo, W, S, and Se, respectively, and were supplied in a gas phase into a one-inch quartz tube furnace by the help of bubbler system with Ar as a carrier gas. The MoS_2 flakes were synthesized on a 300 nm-thick SiO_2/Si wafer with a flow rate of 100 sccm for Ar, 0.1 sccm for $Mo(CO)_6$, and 1.0 sccm for $(C_2H_5)_2S$ under a growth temperature below 350 °C and growth time of 6 h. The WSe_2 flakes were synthesized using a flow rate of 100 sccm of Ar, 1 sccm of H_2, 0.3 sccm of $W(CO)_6$, and 0.05 sccm of $(CH_3)_2Se$ for 5 h under a growth temperature of 420 °C. After growth, the furnace heat was turned down until it reached room temperature. Raman and PL measurements were used to identify the monolayer WSe_2 and MoS_2 flakes used in the high-pressure experiments. For MoS_2, the A'_1-E′ frequency difference at 10 K is ∼19 cm^{-1}, the usual value for monolayer MoS_2. The neutral A exciton, A trion, and neutral B exciton (X_B) energies at 10 K are 1.93, 1.89, and 2.07 eV, respectively, for MoS_2 and 1.73, 1.76 eV for WSe_2 (X_B peak was not detected at 10 K) in excellent agreement with literature values.[47,52]

Loading into the DAC. The CVD MoS_2 and WSe_2 monolayers were initially transferred onto a 25 μm silicon substrate coated with a 300 nm thermal silicon oxide, in a region within a 70-diameter disk surrounded by a horseshoe-shaped trench etched through the substrate.[37] Samples were transferred to this substrate via a deterministic pick-up and transfer method[53] in which the CVD-grown samples were picked up from the substrates without applying heat, with the aid of distilled water droplets placed in the vicinity of the samples.[54] To load the sample into the DAC, we followed the methodology described in ref 37 using a home-built micromanipulator system. The loaded sample consisted of regions of isolated MoS_2 and WSe_2 monolayers, as well as a MoS_2/WSe_2 heterostructure region. In this work, we focused on the pressure evolution of the isolated monolayers.

High-Pressure Raman and Photoluminescence Experiment. The high-pressure Raman and photoluminescence experiments were performed with a CryoDAC-ST DAC (Almax EasyLab), using type IIas ultralow fluorescence diamonds with 300 μm culet and preindented (∼100 μm) BeCu gaskets. Raman and photoluminescence spectra were acquired using a confocal microscope spectrometer (Horiba LabRAM HR Evolution) in a backscattering geometry, with a 50× objective lens and 2.33 eV laser excitation. The high-pressure measurements were performed with a laser power of ∼230 μW after objective to avoid sample damage—the power on the sample was probably lower due to absorption from diamond window and the 4:1 methanol/ethanol PTM. Ambient pressure measurements were performed with a laser power of approximately ∼90 μW for the same reason. Pressure was determined from the ruby fluorescence calibration at low-temperatures obtained from ref 41. The Raman and PL spectra were fitted using Voigt functions since we only aimed to reliably estimate position and intensity ratio of the modes with increasing pressure.

Theoretical Calculations. We applied density functional theory formalism[55−57] within the GGA-PBE parametrization for the exchange-correlation functional.[58] Density functional theory calculations were employed with the SIESTA implementation,[57] making use of a relativistic norm conserving Troullier−Martins pseudopotentials[59] in the factorized Kleinman−Bylander form.[60] Spin−orbit coupling[61] was taken into account in all calculations. The self-consistency was considered achieved when the maximum absolute change in the Hamiltonian matrix elements was below 10^{-5} eV. We expanded the Kohn−Sham states in a basis set composed of double-ζ pseudoatomic orbitals of finite range augmented by polarization functions, the DZP basis set, and we chose the generalized gradient approximation (GGA/PBE)[58] for the exchange-correlation functional. The grid for real space integrations was defined by a mesh cutoff of 450 Ryd, and the Brillouin zone was sampled using a k-grid cutoff of 90 Å. The geometries were considered optimized[62] when the maximum force component (not constrained) in any atom was less than 10 meV/Å, and the maximum stress component was smaller than 0.1 GPa. In our calculations, the in-plane pressure is prespecified and achieved by variations in the lattice vector lengths. As for the vertical direction (z-axis), we explicitly apply forces on the top chalcogen atoms while imposing position constraints on the z-components of the bottom ones. The forces are calculated so as to produce a pressure that matches the in-plane value. All conduction bands calculated from DFT were rigidly shifted in order to be in agreement with the experimental results for MoS2[52] and WSe2[63] monolayers. The bands indicated by the red and blue arrows in Figure 4a,b become spin polarized when the effect of the spin orbit coupling in the conduction

https://doi.org/10.1021/acsnano.2c01065
ACS Nano 2022, 16, 8064−8075

bands is taken into account, as done in ref 5. For vibrational properties, DFT calculations were done with the Vienna Ab initio Simulation Package (VASP) code using the projector-augmented wave[64−67] with the PBE exchange-correlation functional. The energy cutoff of the plane-wave basis was set to 600 eV, and the energy convergence was 10^{-8} eV. A vacuum region of 15 Å was used to separate neighboring periodic images. A Γ-centered k-mesh of 8 × 8 × 1 was used. We employed the supercell approach (4 × 4 × 1 cells) with the finite displacement method within VASP in conjunction with the Phonopy package[68] in order to determine the force constants, the phonon dispersions, and the phonon density of states for MoS_2 and WSe_2. For VASP calculations, the hydrostatic pressure on the monolayer was modeled by changing the in-plane lattice vectors (x, y) and the out-of-plane distance (z) between the chalcogen atoms, in order to have an equal pressure in the three directions. For the 3D band structure plot of MoS_2, we used a grid 75 × 75 × 1 of k-points built using the VASPKIT program.[69]

ASSOCIATED CONTENT

Supporting Information

The Supporting Information is available free of charge at https://pubs.acs.org/doi/10.1021/acsnano.2c01065.

Phonon assignment for the 2LA and LA bands for WSe_2: discussion and Figure S1; pressure evolution of LA Raman modes for MoS_2 and WSe_2: discussion and Figure S2; enhancement of the normalized intensities of DRR modes: discussion and Figure S3; assessment of the lack of non-hydrostatic effects/increasing disorder in our experiments: discussion and Figure S4; pressure enhancement of the different modes composing the 2LA band: discussion and Figure S5; evidence of PL quenching with increasing pressure due to the K−Q crossing: discussion and Figure S6; K−Q crossing for WS_2: discussion; Blueshift of B exciton energy with increasing pressure for WSe_2: discussion and Figure S7; symmetrical shape of 2LA band for MoS_2 after K−Q crossing: discussion and Figure S8; broadening of the first-order bands from MoS_2 and WSe_2: discussion and Figure S9; possible additional contributions to the enhancement of DRR bands: discussion and Figures S10−S13 (PDF)

AUTHOR INFORMATION

Corresponding Authors

Luiz G. Pimenta Martins − *Department of Physics, Massachusetts Institute of Technology, Cambridge, Massachusetts 02139, United States;* orcid.org/0000-0001-9777-7999; Email: lmartins@mit.edu

Matheus J. S. Matos − *Departamento de Física, Universidade Federal de Ouro Preto, Ouro Preto 35400-000, Brazil*; Email: matheusmatos@ufop.edu.br

Jing Kong − *Department of Electrical Engineering and Computer Science, Massachusetts Institute of Technology, Cambridge, Massachusetts 02139, United States;* orcid.org/0000-0003-0551-1208; Email: jingkong@mit.edu

Riccardo Comin − *Department of Physics, Massachusetts Institute of Technology, Cambridge, Massachusetts 02139, United States*; Email: rcomin@mit.edu

Authors

Bruno R. Carvalho − *Departamento de Física, Universidade Federal do Rio Grande do Norte, Natal, Rio Grande do Norte 59078-970, Brazil;* orcid.org/0000-0001-5188-8685

Connor A. Occhialini − *Department of Physics, Massachusetts Institute of Technology, Cambridge, Massachusetts 02139, United States*

Natália P. Neme − *Zernike Institute for Advanced Materials and Stratingh Institute for Chemistry, University of Groningen, 9747 AG Groningen, The Netherlands;* orcid.org/0000-0002-7978-2134

Ji-Hoon Park − *Department of Electrical Engineering and Computer Science, Massachusetts Institute of Technology, Cambridge, Massachusetts 02139, United States*

Qian Song − *Department of Physics, Massachusetts Institute of Technology, Cambridge, Massachusetts 02139, United States*

Pedro Venezuela − *Instituto de Física, Universidade Federal Fluminense, Niterói, Rio de Janeiro 24210-346, Brazil*

Mário S. C. Mazzoni − *Departamento de Física, Universidade Federal de Minas Gerais, Belo Horizonte, Minas Gerais 31270-901, Brazil;* orcid.org/0000-0001-5897-6936

Complete contact information is available at: https://pubs.acs.org/10.1021/acsnano.2c01065

Author Contributions

L.G.P.M., J.K., and R.C. conceived the project. J.K. and R.C. supervised the project. L.G.P.M., J.-H.P., and Q.S. prepared the TMD samples on silicon substrate. L.G.P.M. and C.A.O. carried out the high-pressure Raman and PL experiments. L.G.P.M., B.R.C., and C.A.O. analyzed the experimental data. M.J.S.M., N.P.N., M.S.C.M., and P.V. carried out the DFT calculations. L.G.P.M., B.R.C., M.S.C.M., J.K., and R.C. wrote the manuscript. All authors contributed to scientific discussions and data interpretation.

Notes

The authors declare no competing financial interest.

ACKNOWLEDGMENTS

L.G.P.M., J.-H.P., and J.K. acknowledge the support from the MURI Project by the U.S. Army Research Office (ARO) under Grant No. W911NF-18-1-0431. L.G.P.M. and J.K. acknowledge the support from CNPq under the program Ciência sem Fronteiras (206251/2014-9). This work was performed in part at the Center for Nanoscale Systems (CNS), a member of the National Nanotechnology Coordinated Infrastructure Network (NNCI), which is supported by the National Science Foundation under NSF Award No. 1541959. B.R.C., M.J.S.M., M.S.C.M., and N.P.N. acknowledge financial support from CNPq, CAPES, Fapemig, and INCT-Nano-Carbono. M.J.S.M. also acknowledges support from UFOP. We would like to thank the Center for Information Technology of the University of Groningen for their support and for providing access to the Peregrine high performance computing cluster.

REFERENCES

(1) Wang, Q. H.; Kalantar-Zadeh, K.; Kis, A.; Coleman, J. N.; Strano, M. S. Electronics and optoelectronics of two-dimensional transition metal dichalcogenides. *Nat. Nanotechnol.* **2012**, *7*, 699−712.

(2) Schaibley, J. R.; Yu, H.; Clark, G.; Rivera, P.; Ross, J. S.; Seyler, K. L.; Yao, W.; Xu, X. Valleytronics in 2D materials. *Nat. Rev. Mater.* **2016**, *1*, 16055.

(3) Mak, K. F.; Lee, C.; Hone, J.; Shan, J.; Heinz, T. F. Atomically thin MoS_2: a new direct-gap semiconductor. *Phys. Rev. Lett.* **2010**, *105*, 136805.

(4) Wu, Z.; Xu, S.; Lu, H.; Khamoshi, A.; Liu, G.-B.; Han, T.; Wu, Y.; Lin, J.; Long, G.; He, Y.; Cai, Y.; Yao, Y.; Zhang, F.; Wang, N. Even−odd layer-dependent magnetotransport of high-mobility Q-valley electrons in transition metal disulfides. *Nat. Commun.* **2016**, *7*, 1−8.
(5) Kormányos, A.; Burkard, G.; Gmitra, M.; Fabian, J.; Zólyomi, V.; Drummond, N. D.; Fal'ko, V. k· p theory for two-dimensional transition metal dichalcogenide semiconductors. *2D Mater.* **2015**, *2*, 022001.
(6) Zhu, Z. Y.; Cheng, Y. C.; Schwingenschlögl, U. Giant spin-orbit-induced spin splitting in two-dimensional transition-metal dichalcogenide semiconductors. *Phys. Rev. B* **2011**, *84*, 153402.
(7) Xiao, D.; Liu, G.-B.; Feng, W.; Xu, X.; Yao, W. Coupled spin and valley physics in monolayers of MoS_2 and other group-VI dichalcogenides. *Phys. Rev. Lett.* **2012**, *108*, 196802.
(8) Mak, K. F.; McGill, K. L.; Park, J.; McEuen, P. L. The valley Hall effect in MoS_2 transistors. *Science* **2014**, *344*, 1489−1492.
(9) Barré, E.; Incorvia, J. A. C.; Kim, S. H.; McClellan, C. J.; Pop, E.; Wong, H.-S. P.; Heinz, T. F. Spatial separation of carrier spin by the valley Hall effect in monolayer WSe_2 transistors. *Nano Lett.* **2019**, *19*, 770−774.
(10) Srivastava, A.; Sidler, M.; Allain, A. V.; Lembke, D. S.; Kis, A.; Imamoğlu, A. Valley Zeeman effect in elementary optical excitations of monolayer WSe_2. *Nat. Phys.* **2015**, *11*, 141−147.
(11) MacNeill, D.; Heikes, C.; Mak, K. F.; Anderson, Z.; Kormányos, A.; Zólyomi, V.; Park, J.; Ralph, D. C. Breaking of valley degeneracy by magnetic field in monolayer $MoSe_2$. *Phys. Rev. Lett.* **2015**, *114*, 037401.
(12) Liu, G.-B.; Xiao, D.; Yao, Y.; Xu, X.; Yao, W. Electronic structures and theoretical modelling of two-dimensional group-VIB transition metal dichalcogenides. *Chem. Soc. Rev.* **2015**, *44*, 2643−2663.
(13) Liu, H.; Chen, J.; Yu, H.; Yang, F.; Jiao, L.; Liu, G.-B.; Ho, W.; Gao, C.; Jia, J.; Yao, W.; Xie, M. Observation of intervalley quantum interference in epitaxial monolayer tungsten diselenide. *Nat. Commun.* **2015**, *6*, 1−6.
(14) Ge, Y.; Wan, W.; Feng, W.; Xiao, D.; Yao, Y. Effect of doping and strain modulations on electron transport in monolayer MoS_2. *Phys. Rev. B* **2014**, *90*, 035414.
(15) Piatti, E.; De Fazio, D.; Daghero, D.; Tamalampudi, S. R.; Yoon, D.; Ferrari, A. C.; Gonnelli, R. S. Multi-valley superconductivity in ion-gated MoS_2 layers. *Nano Lett.* **2018**, *18*, 4821−4830.
(16) Piatti, E.; Romanin, D.; Gonnelli, R. S. Mapping multi-valley Lifshitz transitions induced by field-effect doping in strained MoS_2 nanolayers. *J. Phys.: Condens. Matter* **2019**, *31*, 114002.
(17) Ge, Y.; Liu, A. Y. Phonon-mediated superconductivity in electron-doped single-layer MoS_2: a first-principles prediction. *Phys. Rev. B* **2013**, *87*, 241408.
(18) Fu, L.; Wan, Y.; Tang, N.; Ding, Y.-m.; Gao, J.; Yu, J.; Guan, H.; Zhang, K.; Wang, W.; Zhang, C.; Shi, J.-j.; Wu, X.; Shi, S.-F.; Ge, W.; Dai, L.; Shen, B. K-Λ crossover transition in the conduction band of monolayer MoS_2 under hydrostatic pressure. *Sci. Adv.* **2017**, *3*, No. e1700162.
(19) Carvalho, B. R.; Wang, Y.; Mignuzzi, S.; Roy, D.; Terrones, M.; Fantini, C.; Crespi, V. H.; Malard, L. M.; Pimenta, M. A. Intervalley scattering by acoustic phonons in two-dimensional MoS_2 revealed by double-resonance Raman spectroscopy. *Nat. Commun.* **2017**, *8*, 1−8.
(20) Sohier, T.; Ponomarev, E.; Gibertini, M.; Berger, H.; Marzari, N.; Ubrig, N.; Morpurgo, A. F. Enhanced electron-phonon interaction in multivalley materials. *Phys. Rev. X* **2019**, *9*, 031019.
(21) Nguyen, P. V.; Teutsch, N. C.; Wilson, N. P.; Kahn, J.; Xia, X.; Graham, A. J.; Kandyba, V.; Giampietri, A.; Barinov, A.; Constantinescu, G. C.; et al. Visualizing electrostatic gating effects in two-dimensional heterostructures. *Nature* **2019**, *572*, 220−223.
(22) Ye, Y.; Dou, X.; Ding, K.; Jiang, D.; Yang, F.; Sun, B. Pressure-induced K−Λ crossing in monolayer WSe_2. *Nanoscale* **2016**, *8*, 10843−10848.
(23) Fu, X.; Li, F.; Lin, J.-F.; Gong, Y.; Huang, X.; Huang, Y.; Han, B.; Zhou, Q.; Cui, T. Pressure-dependent light emission of charged and neutral excitons in monolayer $MoSe_2$. *J. Phys. Chem. Lett.* **2017**, *8*, 3556−3563.
(24) Gontijo, R. N.; Resende, G. C.; Fantini, C.; Carvalho, B. R. Double resonance Raman scattering process in 2D materials. *J. Mater. Res.* **2019**, *34*, 1976−1992.
(25) Ferrari, A. C.; Basko, D. M. Raman spectroscopy as a versatile tool for studying the properties of graphene. *Nat. Nanotechnol.* **2013**, *8*, 235−246.
(26) Chen, C.-F.; Park, C.-H.; Boudouris, B. W.; Horng, J.; Geng, B.; Girit, C.; Zettl, A.; Crommie, M. F.; Segalman, R. A.; Louie, S. G.; et al. Controlling inelastic light scattering quantum pathways in graphene. *Nature* **2011**, *471*, 617−620.
(27) Kalbac, M.; Reina-Cecco, A.; Farhat, H.; Kong, J.; Kavan, L.; Dresselhaus, M. S. The influence of strong electron and hole doping on the Raman intensity of chemical vapor-deposition graphene. *ACS Nano* **2010**, *4*, 6055−6063.
(28) Cançado, L. G.; Jorio, A.; Ferreira, E. M.; Stavale, F.; Achete, C. A.; Capaz, R. B.; Moutinho, M. V. d. O.; Lombardo, A.; Kulmala, T.; Ferrari, A. C. Quantifying defects in graphene via Raman spectroscopy at different excitation energies. *Nano Lett.* **2011**, *11*, 3190−3196.
(29) Carvalho, B. R.; Pimenta, M. A. Resonance Raman spectroscopy in semiconducting transition-metal dichalcogenides: basic properties and perspectives. *2D Mater.* **2020**, *7*, 042001.
(30) Yoon, D.; Son, Y.-W.; Cheong, H. Strain-dependent splitting of the double-resonance Raman scattering band in graphene. *Phys. Rev. Lett.* **2011**, *106*, 155502.
(31) Huang, M.; Yan, H.; Heinz, T. F.; Hone, J. Probing strain-induced electronic structure change in graphene by Raman spectroscopy. *Nano Lett.* **2010**, *10*, 4074−4079.
(32) Jorio, A.; Dresselhaus, M. S.; Saito, R.; Dresselhaus, G. *Raman Spectroscopy in Graphene Related Systems*; John Wiley & Sons: Weinheim, Germany, 2011.
(33) Frey, G. L.; Tenne, R.; Matthews, M. J.; Dresselhaus, M.; Dresselhaus, G. Raman and resonance Raman investigation of MoS_2 nanoparticles. *Phys. Rev. B* **1999**, *60*, 2883.
(34) Gontijo, R. N.; Gadelha, A.; Silveira, O. J.; Carvalho, B. R.; Nunes, R. W.; Campos, L. C.; Pimenta, M. A.; Righi, A.; Fantini, C. Temperature dependence of the double-resonance Raman bands in monolayer MoS_2. *J. Raman Spectrosc.* **2019**, *50*, 1867−1874.
(35) Del Corro, E.; Terrones, H.; Elias, A.; Fantini, C.; Feng, S.; Nguyen, M. A.; Mallouk, T. E.; Terrones, M.; Pimenta, M. A. Excited excitonic states in 1L, 2L, 3L, and bulk WSe_2 observed by resonant Raman spectroscopy. *ACS Nano* **2014**, *8*, 9629−9635.
(36) del Corro, E.; Botello-Méndez, A.; Gillet, Y.; Elias, A. L.; Terrones, H.; Feng, S.; Fantini, C.; Rhodes, D.; Pradhan, N.; Balicas, L.; et al. Atypical exciton−phonon interactions in WS_2 and WSe_2 monolayers revealed by resonance Raman spectroscopy. *Nano Lett.* **2016**, *16*, 2363−2368.
(37) Pimenta Martins, L. G.; Silva, D. L.; Smith, J. S.; Lu, A.-Y.; Su, C.; Hempel, M.; Occhialini, C.; Ji, X.; Pablo, R.; Alencar, R. S.; Souza, A. C.R.; Pinto, A. A.; de Oliveira, A. B.; Batista, R. J.C.; Palacios, T.; Mazzoni, M. S.C.; Matos, M. J.S.; Comin, R.; Kong, J.; Cancado, L. G. Hard, transparent, sp3-containing 2D phase formed from few-layer graphene under compression. *Carbon* **2021**, *173*, 744−757.
(38) Nayak, A. P.; Pandey, T.; Voiry, D.; Liu, J.; Moran, S. T.; Sharma, A.; Tan, C.; Chen, C.-H.; Li, L.-J.; Chhowalla, M.; et al. Pressure-dependent optical and vibrational properties of monolayer molybdenum disulfide. *Nano Lett.* **2015**, *15*, 346−353.
(39) Machon, D.; Bousige, C.; Alencar, R.; Torres-Dias, A.; Balima, F.; Nicolle, J.; de Sousa Pinheiro, G.; Souza Filho, A. G.; San-Miguel, A. Raman scattering studies of graphene under high pressure. *J. Raman Spectrosc.* **2018**, *49*, 121−129.
(40) Tateiwa, N.; Haga, Y. Evaluations of pressure-transmitting media for cryogenic experiments with diamond anvil cell. *Rev. Sci. Instrum.* **2009**, *80*, 123901.
(41) Feng, Y.; Jaramillo, R.; Wang, J.; Ren, Y.; Rosenbaum, T. Invited article: High-pressure techniques for condensed matter physics at low temperature. *Rev. Sci. Instrum.* **2010**, *81*, 041301.

https://doi.org/10.1021/acsnano.2c01065
ACS Nano 2022, 16, 8064−8075

(42) Mignuzzi, S.; Pollard, A. J.; Bonini, N.; Brennan, B.; Gilmore, I. S.; Pimenta, M. A.; Richards, D.; Roy, D. Effect of disorder on Raman scattering of single-layer MoS_2. *Phys. Rev. B* **2015**, *91*, 195411.
(43) Fujisawa, K.; Carvalho, B. R.; Zhang, T.; Perea-López, N.; Lin, Z.; Carozo, V.; Ramos, S. L.; Kahn, E.; Bolotsky, A.; Liu, H.; et al. Quantification and Healing of Defects in Atomically Thin Molybdenum Disulfide: Beyond the Controlled Creation of Atomic Defects. *ACS Nano* **2021**, *15*, 9658−9669.
(44) Martins Ferreira, E. H.; Moutinho, M. V. O.; Stavale, F.; Lucchese, M. M.; Capaz, R. B.; Achete, C. A.; Jorio, A. Evolution of the Raman spectra from single-, few-, and many-layer graphene with increasing disorder. *Phys. Rev. B* **2010**, *82*, 125429.
(45) Zhou, Y.; Scuri, G.; Wild, D. S.; High, A. A.; Dibos, A.; Jauregui, L. A.; Shu, C.; De Greve, K.; Pistunova, K.; Joe, A. Y.; et al. Probing dark excitons in atomically thin semiconductors via near-field coupling to surface plasmon polaritons. *Nat. Nanotechnol.* **2017**, *12*, 856−860.
(46) Brem, S.; Ekman, A.; Christiansen, D.; Katsch, F.; Selig, M.; Robert, C.; Marie, X.; Urbaszek, B.; Knorr, A.; Malic, E. Phonon-assisted photoluminescence from indirect excitons in monolayers of transition-metal dichalcogenides. *Nano Lett.* **2020**, *20*, 2849−2856.
(47) Arora, A.; Koperski, M.; Nogajewski, K.; Marcus, J.; Faugeras, C.; Potemski, M. Excitonic resonances in thin films of WSe_2: from monolayer to bulk material. *Nanoscale* **2015**, *7*, 10421−10429.
(48) Molina-Sanchez, A.; Wirtz, L. Phonons in single-layer and few-layer MoS 2 and WS 2. *Phys. Rev. B* **2011**, *84*, 155413.
(49) Horzum, S.; Sahin, H.; Cahangirov, S.; Cudazzo, P.; Rubio, A.; Serin, T.; Peeters, F. Phonon softening and direct to indirect band gap crossover in strained single-layer MoSe 2. *Phys. Rev. B* **2013**, *87*, 125415.
(50) Chang, C.-H.; Fan, X.; Lin, S.-H.; Kuo, J.-L. Orbital analysis of electronic structure and phonon dispersion in MoS_2, $MoSe_2$, WS_2, and WSe_2 monolayers under strain. *Phys. Rev. B* **2013**, *88*, 195420.
(51) Park, J.-H.; Lu, A.-Y.; Shen, P.-C.; Shin, B. G.; Wang, H.; Mao, N.; Xu, R.; Jung, S. J.; Ham, D.; Kern, K.; et al. Synthesis of High-Performance Monolayer Molybdenum Disulfide at Low Temperature. *Small Methods* **2021**, *5*, 2000720.
(52) Vaquero, D.; Clericò, V.; Salvador-Sánchez, J.; Martín-Ramos, A.; Díaz, E.; Domínguez-Adame, F.; Meziani, Y. M.; Diez, E.; Quereda, J. Excitons, trions and Rydberg states in monolayer MoS_2 revealed by low-temperature photocurrent spectroscopy. *Commun. Phys.* **2020**, *3*, 1−8.
(53) Wang, J. I.-J.; Yang, Y.; Chen, Y.-A.; Watanabe, K.; Taniguchi, T.; Churchill, H. O.; Jarillo-Herrero, P. Electronic transport of encapsulated graphene and WSe_2 devices fabricated by pick-up of prepatterned hBN. *Nano Lett.* **2015**, *15*, 1898−1903.
(54) Paradisanos, I.; Shree, S.; George, A.; Leisgang, N.; Robert, C.; Watanabe, K.; Taniguchi, T.; Warburton, R. J.; Turchanin, A.; Marie, X.; Gerber, I. C.; Urbaszek, B. Controlling interlayer excitons in MoS_2 layers grown by chemical vapor deposition. *Nat. Commun.* **2020**, *11*, 1−7.
(55) Hohenberg, P.; Kohn, W. Inhomogeneous electron gas. *Phys. Rev.* **1964**, *136*, B864.
(56) Kohn, W.; Sham, L. J. Self-Consistent Equations Including Exchange and Correlation Effects. *Phys. Rev.* **1965**, *140*, A1133−A1138.
(57) Soler, J. M.; Artacho, E.; Gale, J. D.; García, A.; Junquera, J.; Ordejón, P.; Sánchez-Portal, D. The SIESTA method for ab initio order-N materials simulation. *J. Phys.: Condens. Matter* **2002**, *14*, 2745.
(58) Perdew, J. P.; Burke, K.; Ernzerhof, M. Generalized gradient approximation made simple. *Phys. Rev. Lett.* **1996**, *77*, 3865.
(59) Troullier, N.; Martins, J. L. Efficient pseudopotentials for plane-wave calculations. *Phys. Rev. B* **1991**, *43*, 1993−2006.
(60) Kleinman, L.; Bylander, D. Efficacious form for model pseudopotentials. *Phys. Rev. Lett.* **1982**, *48*, 1425.
(61) Fernandez-Seivane, L.; Oliveira, M. A.; Sanvito, S.; Ferrer, J. On-site approximation for spin−orbit coupling in linear combination of atomic orbitals density functional methods. *J. Phys.: Condens. Matter* **2006**, *18*, 7999.
(62) Moreno, J.; Soler, J. M. Optimal meshes for integrals in real- and reciprocal-space unit cells. *Phys. Rev. B* **1992**, *45*, 13891−13898.
(63) Arora, A.; Koperski, M.; Nogajewski, K.; Marcus, J.; Faugeras, C.; Potemski, M. Excitonic resonances in thin films of WSe_2: from monolayer to bulk material. *Nanoscale* **2015**, *7*, 10421−10429.
(64) Blöchl, P. E. Projector augmented-wave method. *Phys. Rev. B* **1994**, *50*, 17953−17979.
(65) Kresse, G.; Joubert, D. From ultrasoft pseudopotentials to the projector augmented-wave method. *Phys. Rev. B* **1999**, *59*, 1758−1775.
(66) Kresse, G.; Furthmüller, J. Efficient iterative schemes for ab initio total-energy calculations using a plane-wave basis set. *Phys. Rev. B* **1996**, *54*, 11169−11186.
(67) Kresse, G.; Furthmüller, J. Efficiency of ab-initio total energy calculations for metals and semiconductors using a plane-wave basis set. *Comput. Mater. Sci.* **1996**, *6*, 15−50.
(68) Togo, A.; Tanaka, I. First principles phonon calculations in materials science. *Scripta Materialia* **2015**, *108*, 1−5.
(69) Wang, V.; Xu, N.; Liu, J.-C.; Tang, G.; Geng, W.-T. VASPKIT: A user-friendly interface facilitating high-throughput computing and analysis using VASP code. *Comput. Phys. Commun.* **2021**, *267*, 108033.

https://doi.org/10.1021/acsnano.2c01065
ACS Nano 2022, 16, 8064−8075